Visualization of Electron Density Changes Along Chemical Reaction Pathways

Chance Lander,[1] Vardhan Satalkar,[1] Junjie Yang,[1, 2, 3] Xiaoliang Pan,[1] Zheng Pei,[1] Aayushi Chatterji,[1] Chungen Liu,[2] Kenneth M. Nicholas,[1] Robert H. Cichewicz,[1] Zhibo Yang,[1, a)] and Yihan Shao[1, b)]

[1)] *Department of Chemistry and Biochemistry, University of Oklahoma, Norman, Oklahoma 73019, USA*[c)]

[2)] *School of Chemistry and Chemical Engineering, Nanjing University, Nanjing 210046, China.*

[3)] *Division of Chemistry and Chemical Engineering, California Institute of Technology, Pasadena, California 91125, USA*

We propose a simple procedure for visualizing the electron density changes (EDC) during a chemical reaction, which is based on a mapping of rectangular grid points for a stationary structure into (distorted) positions around atoms of another stationary structure. Specifically, during a small step along the minimum energy pathway (MEP), the displacement of each grid point is obtained as a linear combination of the motion of all atoms, with the contribution from each atom scaled by the corresponding Hirshfeld weight. For several reactions (identity S_N2, Claisen rearrangement, Diels-Alder reaction, [3+2] cycloaddition, and phenylethyl mercaptan attack on pericosine A), our EDC plots showed an expected reduction of electron densities around severed bonds (or those with the bond-order lowered), with the opposite observed for newly-formed or enhanced chemical bonds. The EDC plots were also shown for copper triflate catalyzed N_2O fragmentation, where the N–O bond weakening initially occurred on a singlet surface, but continued on a triplet surface after reaching the minimum-energy crossing point (MECP) between the two potential energy surfaces.

I. INTRODUCTION

In chemical reactions, the electron density of a molecular system undergoes significant changes. For simple reactions, such as identity S_N2 and Menshutkin reactions, electron density decreases around broken bonds, whereas the density increases at newly-formed chemical bonds. For other reactions, such as Claisen rearrangement and Diels-Alder reactions, density changes are also expected around double bonds converted into single bonds (or vice versa). *It would be highly desirable to be able to directly visualize such electron density changes (EDC) during a chemical reaction.* However, the EDC visualization is not as straightforward as it seems. In computational chemistry, the electron density of each stationary structure (reactant, transition state, and product) of a reaction can be readily computed on a rectangular grid, and then visualized *via* an isosurface representation. Naively, one can compute the EDC from one stationary structure to another by subtracting the density values on the same rectangular grid. But, the corresponding isosurface plot tells us more about the displacement of each atom (which we already know) than the actual change in the density around key atoms and bonds.

In this work, we aim to develop a simple procedure for enabling the EDC visualization. Before proceeding to introduce our procedure, however, we would like to point out that numerous electron structure-based tools have been developed for analyzing chemical reactions. Below we briefly mention some of these tools, which we would loosely classify into atomic-population-based, bond-order/energy-based, and topology-based ones. The readers are referred to reviews for many other available tools.[1–4]

Atomic charge populations are the intuitive coarse-grained representation of the electronic density.[5] But they are not uniquely defined, practically leading to numerous procedures for computing these charges.[6] These procedures include the decomposition of the one-particle density matrix (actually its product with the overlap matrix, leading to Mulliken and Löwdin charges[7,8]), the partitioning of the electronic density (such as the Bader Atom-in-Molecule charges[9] and the Hirshfeld and related charges[10,11]), the fitting of electrostatic potentials (such as Merz-Kollman ESP charges[12–14] and CHELPG charges[15]), and the natural bond orbital analysis.[16,17] Besides examining the atomic charge differences between stationary structures, one can also analyze the Fukui functions,[18–20] which are often approximated as the electron density difference between a neutral molecule and its anion/cation. The corresponding "atomic charges" are widely used to identify electrophilic and nucleophilic sites of reactants.

The bond order, especially the one proposed by Mayer,[21] has been widely used to characterize covalent bonds in molecules. The corresponding bond energy, which can be obtained using various schemes to decompose the total energy of a molecule,[22–25] can in principle also be employed to assess the strength change of chemical bonds in a reaction. Separately, the bond order can also be gauged *via* the local vibrational analysis,[26] and a chemical reaction can be analyzed using the related unified reaction valley approach (URVA).[27–29]

[a)] Electronic mail: zhibo.yang@ou.edu
[b)] Electronic mail: yihan.shao@ou.edu
[c)] Chance Lander and Vardhan Satalkar contributed equally to this work.

Topological analyses of electron density, density gradient, and wavefunction based quantities [such as the electron localization function (ELF),[30,31] non-covalent interactions (NCI) analysis,[32] and dynamic Voronoi metropolis sampling (DVMS)[33,34]] have been proposed by several research groups. These tools originated from the idea of partitioning the molecular space into different regions, as in the aforementioned Bader's Atoms-in-Molecule (AIM) theory.[9] The ELF function from Becke and Edgecombe,[30] for instance, can be used to divide the electron density into the core basins connecting two nuclei and valence basins representing non-bonding regions and lone pairs[31] and to study the bond evolution in chemical reactions.[35,36] Similarly, the NCI plot can be used to identity the key non-covalent interaction regions in molecules at the equilibrium geometry and transition states.[32] More recently, the DVMS method[33,34] utilized a metropolis walk in the electron configuration space to acquire wavefunction tiles – signed regions of the wavefunction – that can be followed to visualize the motion of the electrons along a reaction pathway.

Going back to the EDC, which is the main focus of this manuscript, we will propose a simple method for directly *visualizing* EDC (without using wavefunction tiles) during a chemical reaction, which will complement the aforementioned analysis tools. The key step for our EDC visualization, as outlined in Section II, is to map a rectangular grid for the first stationary structure (such as reactant) onto the space of the second stationary structure (such as transition state). Through evaluating the electron density on the distorted grid for the second structure, we can assess/visualize the changes to the electron density on the original rectangular grid for the first structure. Such EDCs will be shown in Section IV for several model reactions, which conform well with our chemical intuition.

We would like to dedicate this article to Prof. Peter Gill, whose elegant and masterly applications of simple and advanced mathematical tools in the field of quantum chemistry have been a great inspiration to Y.S. and other authors. To a large extent, our work is an attempt to follow Peter's example and develop simple mathematical tools to advance the chemical understanding. However, as will become obvious, our grid mapping has a serious shortcoming in that it does not conserve the number of electrons. Hopefully, more rigorous procedures will be developed in the future by readers of this special issue.

II. METHOD

Let us consider two stationary structures, **0** and **1**. We will denote the corresponding atomic coordinates as $\boldsymbol{R}_A^{(0)}$ and $\boldsymbol{R}_A^{(1)}$. The key step is to map a rectangular grid around the first structure, $\boldsymbol{G}_k^{(0)}$, into a distorted grid around the second structure, $\boldsymbol{G}_k^{(1,\text{distorted})}$,

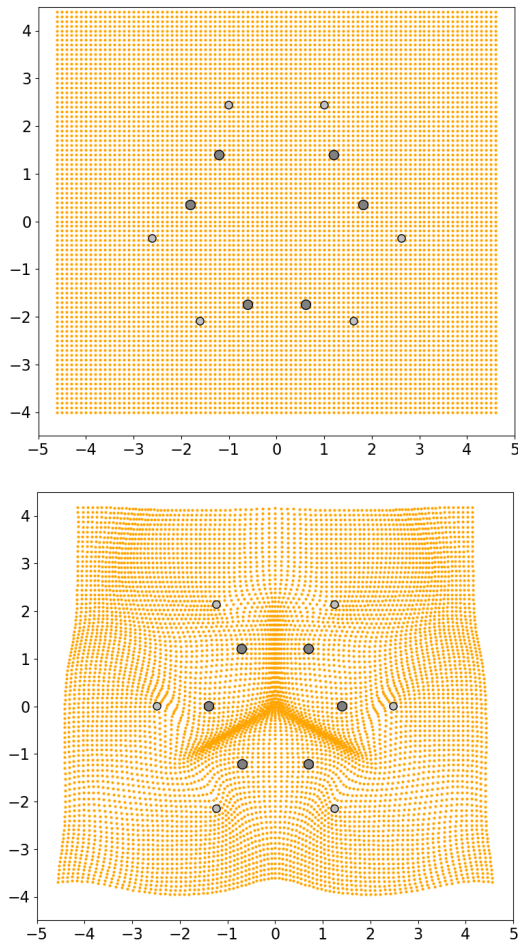$$\boldsymbol{G}_k^{(1,\text{distorted})} = \hat{\mathcal{T}}\, \boldsymbol{G}_k^{(0)} \tag{1}$$

Figure 1: (Top) A rectangular grid (0.1 Å grid size and 2 Å head room) around three acetylene molecules arranged in a hexagonal complex; (Bottom) A distorted grid after transforming onto the benzene molecule. The chemical bonds are not drawn in order to be more clearly see the grid points.

In other words, each grid point in $\boldsymbol{G}_k^{(1,\text{distorted})}$ will be the image of an original point in $\boldsymbol{G}_k^{(0)}$, which results from the molecular structure change.

Let us use the transformation of three acetylene molecules to benzene as an example to illustrate what a mapped grid should look like. The top panel of Fig. 1 shows a rectangular grid (with a 0.1 Å grid size) around three acetylene molecules arranged in a hexagonal complex. Clearly, there are fewer grid points between the two carbon atoms within each acetylene molecule (separated by 1.215 Å) than between the closest carbon atoms from neighboring molecules (distance: 2.410 Å). As the distance between the acetylene molecules shortens to 1.398 Å (which is the equilibrium C–C bond length of benzene), we expect the grid points between these molecules to be squeezed closer to each other, as shown in the bottom panel of Fig. 1. Meanwhile, the C–C bond within each

acetylene molecule gets stretched, so one would expect a larger spacing between the grid points between the two carbon atoms of each acetylene molecule.
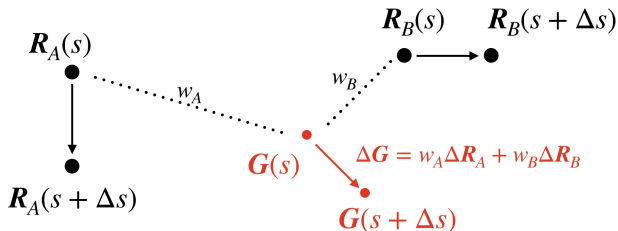

Figure 2: Illustration of the displacement of a grid point based on its weights associated with two atoms in a molecule.

There might be different ways for carrying out such mapping of a rectangular grid into a distorted one. In this work, we will utilize a continuous reaction pathway $\boldsymbol{R}_A(s)$ that connects the two stationary structures, $\boldsymbol{R}_A^{(0)}$ ($s=0$) and $\boldsymbol{R}_A^{(1)}$ ($s=1$). This allows us to implement the mapping in Eq. (1) as

$$\boldsymbol{G}_k^{(1,\text{distorted})} = \boldsymbol{G}_k^{(0)} + \int_0^1 \mathrm{d}s \sum_A w_{A,k}(s) \frac{\mathrm{d}\boldsymbol{R}_A(s)}{\mathrm{d}s} \quad (2)$$

where $w_{A,k}(s)$ refer to a set of atomic weights for each grid point $\boldsymbol{G}_k(s)$ at a given structure along the reaction pathway. For a discretized pathway, this can be carried out with

$$\begin{aligned} &\boldsymbol{G}_k^{\text{distorted}}(s + \Delta s) \\ &= \boldsymbol{G}_k^{\text{distorted}}(s) + \sum_A w_{A,k}(s) \left[\boldsymbol{R}_A(s + \Delta s) - \boldsymbol{R}_A(s) \right] \end{aligned}$$
$$(3)$$

which is illustrated in Fig. 2. Furthermore, in this work, we will adopt the Hirshfeld function for the atomic weights[10]

$$w_{A,k}(s) = \frac{\rho_A^{(\text{free})} \left(|\boldsymbol{G}_k(s) - \boldsymbol{R}_A(s)| \right)}{\sum_B \rho_B^{(\text{free})} \left(|\boldsymbol{G}_k(s) - \boldsymbol{R}_B(s)| \right)} \quad (4)$$

In this expression, the denominator is the so-called pro-molecule density, which is a sum of atomic densities $\rho_B^{(\text{free})}(\boldsymbol{r})$ from each free atom.

After the mapping, the density changes to each rectangular grid point for structure **0** can be computed as

$$\Delta\rho(\boldsymbol{G}_k^{(0)}) = \rho^{(1)} \left(\boldsymbol{G}_k^{(1,\text{distorted})} \right) - \rho^{(0)} \left(\boldsymbol{G}_k^{(0)} \right) \quad (5)$$

III. COMPUTATIONAL AND IMPLEMENTATION DETAILS

In this work, all the stationary structures (reactants, transition states, and products), the minimum

energy crossing point (MECP), and the reactant pathways are optimized using the density functional theory (DFT).[37–39] Specifically, the ωB97X-D functional[40] and the 6-31+G* basis set[41,42], as implemented in Q-Chem version 5.2,[43] were employed. The transition state (TS) structures were obtained in three steps: (a) build a freezing string between the reactant and product geometries,[44,45] (b) take the highest-energy point along the string, and (c) refine the structure using Baker's partitioned rational-function optimization (P-RFO) method.[46] Subsequent harmonic vibrational frequency analysis was performed to confirm a local minima (no imaginary frequency) for the reactant and product or a saddle point (one imaginary frequency) for the transition state. Intrinsic reaction coordinate (IRC) calculations were carried out to connect the TS to the reactant and product structures. The MECP structure for the spin-crossing reaction was optimized using the algorithm proposed by Harvey and coworkers[47] as implemented in the sobMECP software by Lu (http://sobereva.com/286).

The EDC analysis was carried out using QMAnalysis, a locally developed Python program. For each analysis, it only requires: (a) the Q-Chem checkpoint files for the two end structures (reactant/TS, TS/product, reactant/MECP, or MECP/product); and (b) the pathway file (in xyz format) in between. The QMAnalysis program can be accessed at https://github.com/cc-ats/edc, which is being further developed. The checkpoint and pathway files can also be found in this GitHub repository.

IV. RESULTS

To test our EDC analysis tool, we considered six representative unimolecular and bimolecular reactions: (A) the identity S_N2 reaction; (B) the Claisen rearrangement of allyl vinyl ether; (C) the Diels-Alder cycloaddition between cyclopentadiene and acrylonitrile; (D) the [3+2] cycloaddition of the azomethine ylide pseudoradical with ethylene; (E) the S_N2' reaction between pericosine A and phenylethyl mercaptane; and (F) the splitting of N_2O bound to copper triflate. When multiple bond forming and breaking are involved, some of the above reactions are asynchronous (such as the example Claisen rearrangement, Diels-Alder, and pericosine reactions), whereas others are concerted (such as the identity S_N2 and [3+2] cycloaddition). While most of the reactions are spin-conserving, the last reaction involves a crossing from a singlet surface of the N_2O-Cu-Triflate complex to the triplet one. Besides the EDC plots shown in the following main text, the EDC movies of the studied reactions and the reaction energy profiles can be found in the supporting information (SI).
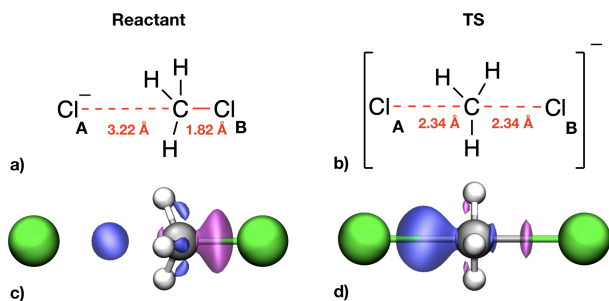
A. Identity S_N2 reaction

Figure 3: (a) Reactant, and (b) transition state of the identity S_N2 reaction between methyl chloride and chloride anion. EDC plots for the (c) reactant to TS and (d) TS to product stages, where the magenta/blue color indicates decrease/increase of electron density. Isovalue for the EDC surface: 0.03.

Bimolecular nucleophilic substitution S_N2 reactions are widely studied both experimentally[48,49] and theoretically.[50–52] Here, we shall use the identity S_N2 reaction between methyl chloride and chloride anion to test our new EDC method. The reactant structure (Fig. 3a) was constructed from two fragments, namely chloride anion (Cl_A^-) and methyl chloride (CH_3Cl_B), which were separated by a Cl_A–C distance of 3.22 Å. The nucleophilic attack of the chloride anion led to the transition state in Fig. 3b. At the transition state, the carbon atom of the methyl chloride is equidistant from two chlorine atoms with both C–Cl_A and C–Cl_B distances being 2.34 Å. From the TS structure, the product was generated with the C-Cl_A bond distance of 1.82 Å, and chloride anion (Cl_B^-) as the leaving group.

Fig. 3c showed the electron density change from the reactant to the transition state. As expected, it showed a decrease in the electron density from the C–Cl_B σ bond (shown in magenta) of methyl chloride and the emergence of a new bond (shown in blue) between Cl_A and the carbon atom of the methyl chloride. In this stage, the three C–H bonds of methyl chloride also gained a minor increase in their electron densities. A complete formation of the Cl_A–C bond (with a large blue cloud) and the further weakening of the C–Cl_B bond could be seen during the subsequent transition from TS to the product in Fig. 3d. Movies showing the EDC for entire pathway can be found in the supporting information for all reactions studied in our work, with sn2_iso02.mp4 for the identity S_N2 reaction.

B. Claisen rearrangement

The [3,3] sigmatropic rearrangement of the allyl vinyl ethers to the γ,δ-unsaturated carbonyl compounds,[53] also
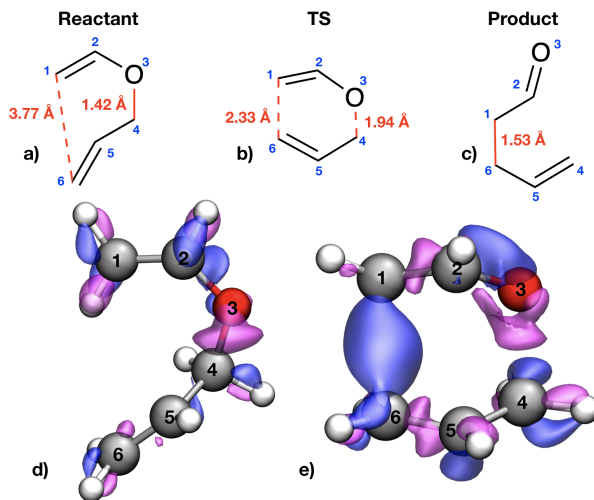

Figure 4: (a) Reactant, (b) transition state, (c) product of the Claisen rearrangement reaction. EDC plots for the (d) reactant to TS and (e) TS to product stages. Isovalue for the EDC surface: 0.05.

known as the Claisen rearrangement or analogous Cope rearrangement,[54,55] were shown in Fig. 4. In the reactant structure, the ether bond C_4–O_3 has a normal bond length of 1.42 Å. As the reaction progressed toward the TS, one observed a lengthening of the C_4–O_3 ether bond from 1.42 Å to 1.94 Å. This was accompanied by a conformational change, namely a change of the O_3–C_4–C_5–C_6 dihedral angle, which reduced the C_1–C_6 distance (between two terminal allyl carbon atoms) from 3.37 to 2.33 Å and resulted in a chair-like TS (Fig. 4e). In the SI Figs. S1 and S2, the chair form of the TS was shown to be 6.0 kcal/mol more stable than the boat form, consistent with previous computational analysis.[56]

The EDC plots in Figs. 4d and 4e showed that the weakening of the C_4–O_3 σ bond (shown in magenta) and the strengthening of the C_2–O_3 bond occurred in both reactant→TS and TS→product stages. On the other hand, the formation of the C_1-C_6 σ bond and the weakening of C_1–C_2 and C_5–C_6 bonds occurred mostly after the TS.

C. Diels-Alder cycloaddition

The [4+2] Diels-Alder cycloaddition between cyclopentadiene and acrylonitrile is well-known for its asynchronous reaction pathway.[57–61] In the reactant structure (Fig. 5a), the cyclopentadiene and acrylonitrile molecules are separated by 3.17–3.24 Å. As the reaction progressed, the two fragments moved closer to each other. At the TS structure (Fig. 5b), the distance between the C_4 carbon of cyclopentadiene and the C_6 carbon of acrylonitrile was reduced to be 2.09 Å. Meanwhile, the C_1–C_7 distance was reduced only to 2.43 Å, suggesting an asynchronous cycloaddition caused by the presence of the
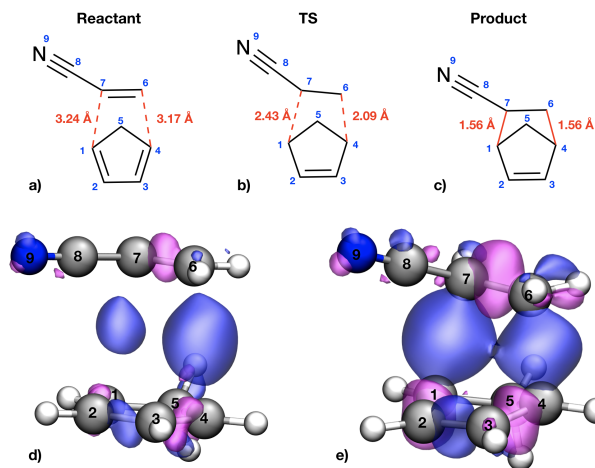
Figure 5: Diels-Alder reaction between cyclopentadiene and acrylonitrile. EDC plots for (d) reactant→TS and (e) TS→product stages. Isovalue for the EDC surface: 0.02.
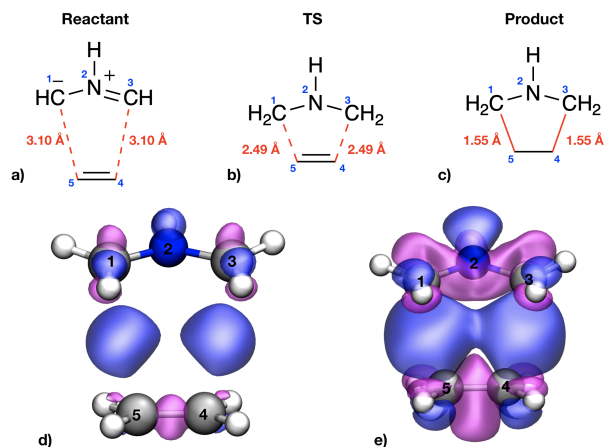

Figure 6: (a) Reactant, (b) transition state, (c) product of the 1,3-dipolar reaction. EDC plots for the (d) reactant to TS and (e) TS to product stages. Isovalue for the EDC surface: 0.01.

cyano group during the distance reduction between the double bond and (gradually nonplanar) cyclopentadiene. After the transition state, the formation of C_4–C_6 bond and C_1–C_7 bonds were both completed, with the final bond distances being 1.56 Å.

As shown in Fig. 5d, the reaction started with a transfer of electrons of three C–C double bonds of acrylonitrile and cyclopentadiene (shown in magenta) to the formation of the C_4–C_6 and C_1–C_7 bonds (shown in blue), respectively. Noticeably, a more substantial electron density change occurred between the C_4 and C_6 atoms, consistent with a short distance at the transition. At the same time, a relatively smaller electron density change was observed between C_1–C_7 atoms, indicating a slower bond formation. In addition to the partial formation of these new σ bonds, the C_2–C_3 bond of the cyclopentadiene also gained electron density, bringing it a partial double-bond character. The EDC from the TS to the product showed the completion of the reaction (Fig. 5e), where the π bond of acrylonitrile (C_6–C_7) is the primary site for losing electrons while C_1–C_2 and C_3–C_4 bonds of cyclopentadiene continued to lose electrons (in magenta). On the other hand, the electron density on the cyano group underwent only marginal changes throughout the reaction.

D. Cycloaddition between azomethine ylide and ethylene

The pseudoradical (pr)-type azomethine ylide and ethylene can undergo the [3+2] cycloaddition to form regioisomeric pyrrolidines.[62,63] Domingo and coworkers suggested that the pseudoradical nature of azomethine ylide is the primary reason for the low activation energy barrier (1.2 kcal/mol) of the above cycloadditon reaction.[64,65] Here, the reactant structure consisted of

two fragments: the azomethine ylide and ethylene (Fig. 6a). The initial distances are 3.10 Å for both C_1–C_5 and C_3–C_4. During the reaction, these fragments came closer, reducing the C_1–C_5 and C_3–C_4 distances from 3.10 Å to 2.49 Å at TS. Subsequently, during the transition from the TS to the product, both bond lengths were further decreased to 1.55 Å. In contrast to the Diels-Alder reaction in Section IV C, this [3+2] cycloaddition reaction proceeded in a concerted fashion.

The EDC plots in panels (d) and (e) of Fig. 6 confirmed the concerted mechanism of this cycloaddition reaction. During the transition from the reactant to TS, the π bond of ethylene and π orbitals of azomethine ylide lost some electron density (shown in magenta). At the same time, two nascent bonds with an equal amount of electron density could be seen (marked blue) between two fragments. During the subsequent transformation from the TS to product, two single bonds between ethylene and azomethine ylide fragments were completely formed (shown in blue), whereas the π orbitals of both ethylene and azomethine ylide orbitals were significant donors of the electron density (shown in magenta).

E. $S_N 2'$ reaction between pericosine A and phenylethyl mercaptan

To neutralize the pungent odor of skunk spray, which arises mainly from mercaptans, Du and coworkers reported a chemoreactive fungal metabolite of *Tolypocladium sp.* termed pericosine A.[66,67] With the help of a Michael acceptor—methoxycarbonyl group—on C_4 and chlorine atom on C_6 position, the pericosine A scaffold can act as an electron sink during its reaction with the nucleophilic mercaptan. The reaction between phenylethyl mercaptan and pericosine A (shown in Fig. 7) was reported to follow two potential mechanisms: *syn*-$S_N 2'$ and
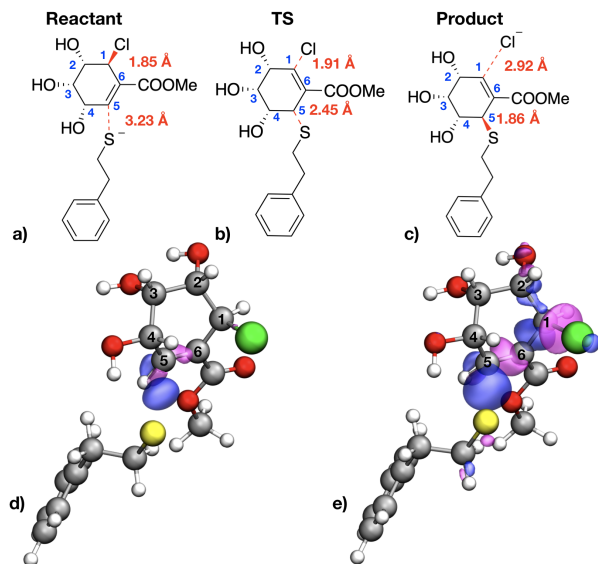
Figure 7: (a) Reactant, (b) transition state, (c) product of the reaction between pericosine A and phenylethyl mercaptan. EDC plots for the (d) reactant to TS and (e) TS to product stages. Isovalue for the EDC surface: 0.02.
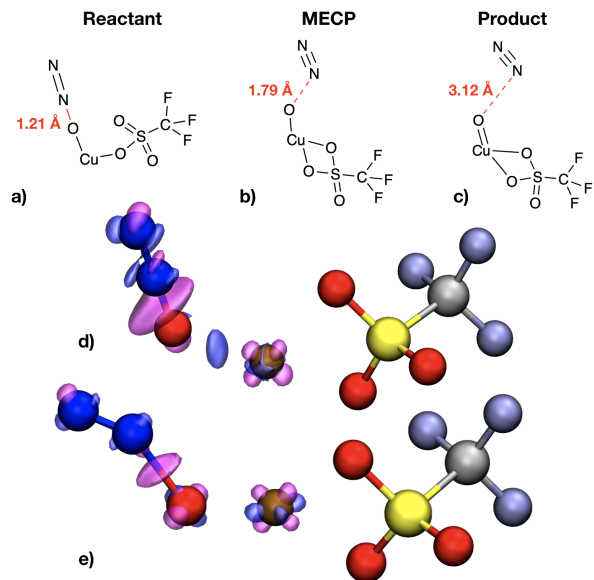

Figure 8: (a) Reactant, (b) transition state, (c) product of the spin-crossing splitting of N_2O bound to copper triflate. EDC plots for the (d) reactant to MECP on the singlet surface and (e) MECP to product on the triplet surface. Isovalue for the EDC surface: 0.05.

anti-S_N2',[66] depending on the stereochemistry of the attack of thiolate on the pericosine molecule. In our calculations, we focused on the syn-S_N2' reaction pathway shown in Fig. S6. At the TS of the syn-S_N2' reaction pathway, the S–C_5 distance was found to be 2.45 Å, and the C_1–Cl bond is 1.91 Å long. During the transition from TS to the products, the S–C_5 bond length decreased from 2.45 to 1.86 Å, whereas the C_1–Cl bond length increased from 1.91 to 2.92 Å.

The EDC plot in Fig. 7 showed the main density changes for the syn-S_N2' reaction mechanism. During the transition from the reactant to TS, the C_5–C_6 π bond lost some electron density (shown in magenta in Fig. 7d), and the new S–C_5 bond was partially formed (shown in blue). From the TS to product, the S–C_5 bond was completely formed, along with a π bond migration from C_5–C_6 to C_6–C_1 in Fig. 7e. Notably, the C_1–Cl bond was broken (shown in magenta) only after the TS, leading to the release of a chloride ion. This is also consistent with the change of bond lengths shown in Fig. S6b.

F. Spin-crossing splitting of N_2O bound to copper triflate

A reaction involving the splitting of N_2O through the cleavage of the N-O bond with a copper(I) triflate has been recently studied using DFT calculations.[68] As shown in Fig. 8, the reactant structure was a singlet state with the copper triflate bound to N_2O. However, the dissociation of N_2O resulted in the production of singlet N_2 and a triplet copper-oxo species. Thus, the overall reaction exhibited a spin-crossing transition from the singlet

reactant state to the triplet product state. This resulted in an MECP as the highest energy point along the reaction path shown in Fig. S7. At MECP, the N-O bond stretched to 1.79 from 1.21 Å, and the N_2O molecule adopted a bent conformation (Figs. 8b and 8e). After the MECP, the reaction proceeded on the triplet surface. When the reaction moved to the product, the N-O bond was fully broken, and the Cu atom was predicted to transition from Cu(I) to Cu(II) oxidation state.

The EDC plot in Fig. 8d showed a cleavage of the N-O bond and strengthening of the Cu–O bond as the reaction moved towards the MECP. After the MECP, the plot in Fig. 8e showed a further decrease in the electron density around the N–O bond and a small increase in the electron density of the N–N bond. Furthermore, the EDC around the copper atom reflected changes in the electron density of d orbitals as the copper transitions between oxidation states.

V. CONCLUSIONS

In this work, we proposed a simple scheme for mapping grid points from one molecular structure to another. Such a mapping allows for a direct visualization of electron density changes (EDC) along the reaction pathway. For six representative reactions, the acquired EDC plots/movies provided intuitive pictures of the (concerted or asynchronous) motion of electrons during the reaction process. Our EDC approach thus provides a handy tool for chemical reaction analysis, which complements many

other existing ones in the toolbox (including the recent DVMS method).

While this work was entirely focused on the electron density, we expect that our grid mapping is applicable to the study of changes to other scalar or vector quantities from quantum chemistry calculations, such as the energy densities[69,70] and the electrostatic potential/field, which can potentially enhance our understanding of reactive and binding processes as well as conformational changes.

We note, however, our grid mapping does not conserve the number of electrons. This is especially obvious in the TOC figure, which shows the EDC during the transformation from three acetylene molecules into benzene. There, the net increase in the electron density between acetylene molecules (marked blue) appears to be more substantial than the decrease of the electron density (shown magenta) along the original C–C triple bond. We believe that, to overcome this, different weights need to be assigned to the points of the original rectangular grid as well as the distorted grid. One can potentially use an auxiliary grid, such as the atom-centered Lebedev grid,[71] and project the corresponding weights onto the rectangular and distorted grids. However, it remains to be tested.

ACKNOWLEDGMENTS

TOC
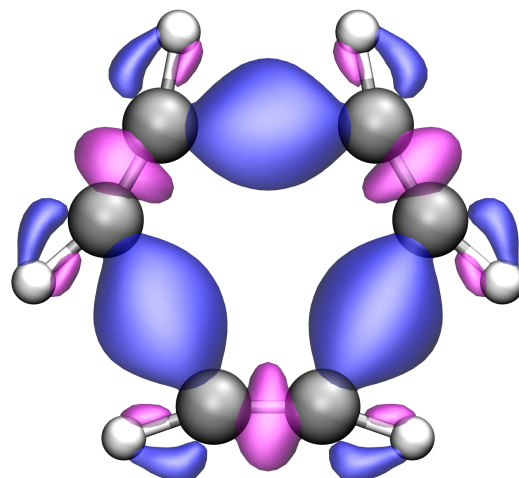
REFERENCES

[1] P. Geerlings, F. De Proft, and W. Langenaeker, "Conceptual density functional theory," Chem. Rev. **103**, 1793 (2003).

[2] L. Domingo, M. Ríos-Gutiérrez, and P. Pérez, "Applications of the conceptual density functional theory indices to organic chemistry reactivity," Mol. **21**, 748 (2016).

[3] M. J. S. Phipps, T. Fox, C. S. Tautermann, and C.-K. Skylaris, "Energy decomposition analysis approaches and their evaluation on prototypical protein–drug interaction patterns," Chem. Soc. Rev. **44**, 3177 (2015).

[4] L. Zhao, M. von Hopffgarten, D. M. Andrada, and G. Frenking, "Energy decomposition analysis," WIREs Comput. Mol. Sci. **8** (2018).

[5] S. Saha, R. K. Roy, and P. W. Ayers, "Are the Hirshfeld and Mulliken population analysis schemes consistent with chemical intuition?: Consistency of HPA and MPA schemes with chemical intuition," Int. J. Quantum Chem. **109**, 1790 (2009).

[6] Y. Mei, A. C. Simmonett, F. C. Pickard, R. A. DiStasio, B. R. Brooks, and Y. Shao, "Numerical study on the partitioning of the molecular polarizability into fluctuating charge and induced atomic dipole contributions," J. Phys. Chem. A **119**, 5865 (2015).

[7] R. S. Mulliken, "Electronic population analysis on LCAO–MO molecular wave functions. I," J. Chem. Phys. **23**, 1833 (1955).

[8] P. Löwdin, "On the non-orthogonality problem connected with the use of atomic wave functions in the theory of molecules and crystals," J. Chem. Phys. **18**, 365 (1950).

[9] R. F. W. Bader, *Atoms in molecules: a quantum theory*, The International series of monographs on chemistry No. 22 (Clarendon Press ; Oxford University Press, Oxford [England] : New York, 1994).

[10] F. L. Hirshfeld, "Bonded-atom fragments for describing molecular charge densities," Theor. Chim. Acta **44**, 129 (1977).

[11] A. V. Marenich, S. V. Jerome, C. J. Cramer, and D. G. Truhlar, "Charge model 5: An extension of Hirshfeld population analysis for the accurate description of molecular interactions in gaseous and condensed Phases," J. Chem. Theory Comput. **8**, 527 (2012).

[12] U. C. Singh and P. A. Kollman, "An approach to computing electrostatic charges for molecules," J. Comput. Chem. **5**, 129 (1984).

[13] B. H. Besler, K. M. Merz, and P. A. Kollman, "Atomic charges derived from semiempirical methods," J. Comput. Chem. **11**, 431 (1990).

[14] W. D. Cornell, P. Cieplak, C. I. Bayly, and P. A. Kollman, "Application of RESP charges to calculate conformational energies,

hydrogen bond energies, and free energies of solvation," J. Am. Chem. Soc. **115**, 9620 (1993).

[15] C. M. Breneman and K. B. Wiberg, "Determining atom-centered monopoles from molecular electrostatic potentials. The need for high sampling density in formamide conformational analysis," J. Comput. Chem. **11**, 361 (1990).

[16] A. E. Reed, R. B. Weinstock, and F. Weinhold, "Natural population analysis," J. Chem. Phys. **83**, 735 (1985).

[17] E. D. Glendening, C. R. Landis, and F. Weinhold, "Natural bond orbital methods," WIREs Comput. Mol. Sci. **2**, 1 (2012).

[18] R. G. Parr and W. Yang, "Density functional approach to the frontier-electron theory of chemical reactivity," J. Am. Chem. Soc. **106**, 4049 (1984).

[19] W. Yang and W. J. Mortier, "The Use of global and local molecular parameters for the analysis of the gas-phase basicity of amines," J. Am. Chem. Soc. **108**, 5708 (1986).

[20] W. Yang, A. J. Cohen, F. De Proft, and P. Geerlings, "Analytical evaluation of Fukui functions and real-space linear response function," J. Chem. Phys. **136**, 144110 (2012).

[21] I. Mayer, "Charge, bond order and valence in the ab initio SCF theory," Chem. Phys. Lett. **97**, 270 (1983).

[22] H. Kollmar, "Partitioning scheme for the ab initio SCF energy," Theoret. Chim. Acta **50**, 235 (1978).

[23] H. Ichikawa and A. Yoshida, "Complete one- and two-center partitioning scheme for the total energy in the Hartree-Fock theory," Int. J. Quant. Chem. **71**, 35 (1999).

[24] I. Mayer, "An exact chemical decomposition scheme for the molecular energy," Chem. Phys. Lett. **382**, 265 (2003).

[25] H. Nakai, H. Ohashi, Y. Imamura, and Y. Kikuchi, "Bond energy analysis revisited and designed toward a rigorous methodology," J. Chem. Phys. **135**, 124105 (2011).

[26] E. Kraka, W. Zou, and Y. Tao, "Decoding chemical information from vibrational spectroscopy data: Local vibrational mode theory," WIREs Comput. Mol. Sci. **10** (2020).

[27] Z. Konkoli, E. Kraka, and D. Cremer, "Unified reaction valley approach mechanism of the reaction $CH_3 + H_2 \rightarrow CH_4 + H$," J. Phys. Chem. A **101**, 1742 (1997).

[28] T. M. Sexton, M. Freindorf, E. Kraka, and D. Cremer, "A reaction valley investigation of the cycloaddition of 1,3-dipoles with the dipolarophiles ethene and acetylene: Solution of a mechanistic puzzle," J. Phys. Chem. A **120**, 8400 (2016).

[29] W. Zou, T. Sexton, E. Kraka, M. Freindorf, and D. Cremer, "A new method for describing the mechanism of a chemical reaction based on the unified reaction valley approach," J. Chem. Theory Comput. **12**, 650 (2016).

[30] A. D. Becke and K. E. Edgecombe, "A simple measure of electron localization in atomic and molecular systems," J. Chem. Phys. **92**, 5397 (1990).

[31] B. Silvi and A. Savin, "Classification of chemical bonds based on topological analysis of electron localization functions," Nature **371**, 683 (1994).

[32] E. R. Johnson, S. Keinan, P. Mori-Sánchez, J. Contreras-García, A. J. Cohen, and W. Yang, "Revealing noncovalent interactions," J. Am. Chem. Soc. **132**, 6498 (2010).

[33] Y. Liu, T. J. Frankcombe, and T. W. Schmidt, "Chemical bonding motifs from a tiling of the many-electron wavefunction," Phys. Chem. Chem. Phys. **18**, 13385 (2016).

[34] Y. Liu, P. Kilby, T. J. Frankcombe, and T. W. Schmidt, "Calculating curly arrows from ab initio wavefunctions," Nat. Commun. **9**, 1436 (2018).

[35] X. Krokidis, S. Noury, and B. Silvi, "Characterization of elementary chemical processes by catastrophe theory," J. Phys. Chem. A **101**, 7277 (1997).

[36] L. R. Domingo, "A new C–C bond formation model based on the quantum chemical topology of electron density," RSC Adv. **4**, 32415 (2014).

[37] R. G. Parr and W. Yang, *Density-functional theory of atoms and molecules*, International series of monographs on chemistry (Oxford Univ. Press, New York, NY, 1994).

[38] K. Burke, "Perspective on density functional theory," J. Chem. Phys. **136**, 150901 (2012).

[39] A. D. Becke, "Perspective: Fifty years of density-functional theory in chemical physics," J. Chem. Phys. **140**, 18A301 (2014).

[40] J.-D. Chai and M. Head-Gordon, "Long-range corrected hybrid density functionals with damped atom-atom dispersion corrections," Phys. Chem. Chem. Phys. **10**, 6615 (2008).

[41] W. J. Hehre, R. Ditchfield, and J. A. Pople, "Self-Consistent Molecular Orbital Methods. XII. Further Extensions of Gaussian-Type Basis Sets for Use in Molecular Orbital Studies of Organic Molecules," J. Chem. Phys. **56**, 2257–2261 (1972).

[42] P. C. Hariharan and J. A. Pople, "The influence of polarization functions on molecular orbital hydrogenation energies," Theor. Chim. Acta **28**, 213 (1973).

[43] E. Epifanovsky, A. T. B. Gilbert, X. Feng, J. Lee, Y. Mao, N. Mardirossian, P. Pokhilko, A. F. White, M. P. Coons, A. L. Dempwolff, Z. Gan, D. Hait, P. R. Horn, L. D. Jacobson, I. Kaliman, J. Kussmann, A. W. Lange, K. U. Lao, D. S. Levine, J. Liu, S. C. McKenzie, A. F. Morrison, K. D. Nanda, F. Plasser, D. R. Rehn, M. L. Vidal, Z.-Q. You, Y. Zhu, B. Alam, B. J. Albrecht, A. Aldossary, E. Alguire, J. H. Andersen, V. Athavale, D. Barton, K. Begam, A. Behn, N. Bellonzi, Y. A. Bernard, E. J. Berquist, H. G. A. Burton, A. Carreras, K. Carter-Fenk, R. Chakraborty, A. D. Chien, K. D. Closser, V. Cofer-Shabica, S. Dasgupta, M. de Wergifosse, J. Deng, M. Diedenhofen, H. Do, S. Ehlert, P.-T. Fang, S. Fatehi, Q. Feng, T. Friedhoff, J. Gayvert, Q. Ge, G. Gidofalvi, M. Goldey, J. Gomes, C. E. González-Espinoza, S. Gulania, A. O. Gunina, M. W. D. Hanson-Heine, P. H. P. Harbach, A. Hauser, M. F. Herbst, M. Hernández Vera, M. Hodecker, Z. C. Holden, S. Houck, X. Huang, K. Hui, B. C. Huynh, M. Ivanov, A. Jász, H. Ji, H. Jiang, B. Kaduk, S. Kähler, K. Khistyaev, J. Kim, G. Kis, P. Klunzinger, Z. Koczor-Benda, J. H. Koh, D. Kosenkov, L. Koulias, T. Kowalczyk, C. M. Krauter, K. Kue, A. Kunitsa, T. Kus, I. Ladjánszki, A. Landau, K. V. Lawler, D. Lefrancois, S. Lehtola, R. R. Li, Y.-P. Li, J. Liang, M. Liebenthal, H.-H. Lin, Y.-S. Lin, F. Liu, K.-Y. Liu, M. Loipersberger, A. Luenser, A. Manjanath, P. Manohar, E. Mansoor, S. F. Manzer, S.-P. Mao, A. V. Marenich, T. Markovich, S. Mason, S. A. Maurer, P. F. McLaughlin, M. F. S. J. Menger, J.-M. Mewes, S. A. Mewes, P. Morgante, J. W. Mullinax, K. J. Oosterbaan, G. Paran, A. C. Paul, S. K. Paul, F. Pavošević, Z. Pei, S. Prager, E. I. Proynov, A. Rák, E. Ramos-Cordoba, B. Rana, A. E. Rask, A. Rettig, R. M. Richard, F. Rob, E. Rossomme, T. Scheele, M. Scheurer, M. Schneider, N. Sergueev, S. M. Sharada, W. Skomorowski, D. W. Small, C. J. Stein, Y.-C. Su, E. J. Sundstrom, Z. Tao, J. Thirman, G. J. Tornai, T. Tsuchimochi, N. M. Tubman, S. P. Veccham, O. Vydrov, J. Wenzel, J. Witte, A. Yamada, K. Yao, S. Yeganeh, S. R. Yost, A. Zech, I. Y. Zhang, X. Zhang, Y. Zhang, D. Zuev, A. Aspuru-Guzik, A. T. Bell, N. A. Besley, K. B. Bravaya, B. R. Brooks, D. Casanova, J.-D. Chai, S. Coriani, C. J. Cramer, G. Cserey, A. E. DePrince, R. A. DiStasio, A. Dreuw, B. D. Dunietz, T. R. Furlani, W. A. Goddard, S. Hammes-Schiffer, T. Head-Gordon, W. J. Hehre, C.-P. Hsu, T.-C. Jagau, Y. Jung, A. Klamt, J. Kong, D. S. Lambrecht, W. Liang, N. J. Mayhall, C. W. McCurdy, J. B. Neaton, C. Ochsenfeld, J. A. Parkhill, R. Peverati, V. A. Rassolov, Y. Shao, L. V. Slipchenko, T. Stauch, R. P. Steele, J. E. Subotnik, A. J. W. Thom, A. Tkatchenko, D. G. Truhlar, T. Van Voorhis, T. A. Wesolowski, K. B. Whaley, H. L. Woodcock, P. M. Zimmerman, S. Faraji, P. M. W. Gill, M. Head-Gordon, J. M. Herbert, and A. I. Krylov, "Software for the frontiers of quantum chemistry: An overview of developments in the Q-Chem 5 package," J. Chem. Phys. **155**, 084801 (2021).

[44] A. Behn, P. M. Zimmerman, A. T. Bell, and M. Head-Gordon, "Efficient exploration of reaction paths via a freezing string method," Chem. Phys. **135**, 224108 (2011).

[45] S. Mallikarjun Sharada, P. M. Zimmerman, A. T. Bell, and M. Head-Gordon, "Automated Transition State Searches without Evaluating the Hessian," J. Chem. Theory Comput. **8**, 5166–5174

(2012).

[46] J. Baker, "An Algorithm for the Location of Transition States," J. Comput. Chem. **7**, 385 (1986).

[47] J. N. Harvey, M. Aschi, H. Schwarz, and W. Koch, "The singlet and triplet states of phenyl cation. A hybrid approach for locating minimum energy crossing points between non-interacting potential energy surfaces," Theor. Chem. Acc. **99**, 95 (1998).

[48] D. K. Bohme and G. I. Mackay, "Bridging the gap between the gas phase and solution: Transition in the kinetics of nucleophilic displacement reactions," J. Am. Chem. Soc. **103**, 978 (1981).

[49] D. K. Bohme and A. B. Raksit, "Gas-phase measurements of the influence of stepwise solvation on the kinetics of nucleophilic displacement reactions with chloromethane and bromomethane at room temperature," J. Am. Chem. Soc. **106**, 3447 (1984).

[50] J. Chandrasekhar, S. F. Smith, and W. L. Jorgensen, "Theoretical examination of the S_N2 reaction involving chloride ion and methyl chloride in the gas phase and aqueous solution," J. Am. Chem. Soc. **107**, 154 (1985).

[51] S. S. Shaik, "Solvent effect on reaction barriers. The S_N2 reaction. 1. Application to the identity exchange," J. Am. Chem. Soc. **106**, 1227 (1984).

[52] S. R. Vande Linde and W. L. Hase, "Trajectory studies of S_N2 nucleophilic substitution. I. Dynamics of Cl^-+CH_3Cl reactive collisions," Chem. Phys. **93**, 7962 (1990).

[53] L. Claisen, "Über umlagerung von phenol-allyläthern in C -allyl-phenole," Ber. Dtsch. Chem. Ges. **45**, 3157 (1912).

[54] A. C. Cope and E. M. Hardy, "The Introduction of Substituted Vinyl Groups. V. A Rearrangement Involving the Migration of an Allyl Group in a Three-Carbon System ^{1}," J. Am. Chem. Soc. **62**, 441–444 (1940).

[55] A. M. Martín Castro, "Claisen rearrangement over the past nine decades," Chem. Rev. **104**, 2939 (2004).

[56] R. L. Vance, N. G. Rondan, K. N. Houk, F. Jensen, W. T. Borden, A. Komornicki, and E. Wimmer, "Transition structures for the claisen rearrangement," J. Am. Chem. Soc. **110**, 2314 (1988).

[57] A. I. Konovalov, G. I. Kamasheva, and M. P. Loskutow, J. Org. Chem. USSR **9**, 2064 (1973).

[58] K. N. Houk, R. J. Loncharich, J. F. Blake, and W. L. Jorgensen, "Substituent effects and transition structures for Diels-Alder reactions of butadiene and cyclopentadiene with cyanoalkenes," J. Am. Chem. Soc. **111**, 9172 (1989).

[59] W. L. Jorgensen, D. Lim, and J. F. Blake, "Ab initio study of Diels-Alder reactions of cyclopentadiene with ethylene, isoprene, cyclopentadiene, acrylonitrile, and methyl vinyl ketone," J. Am. Chem. Soc. **115**, 2936 (1993).

[60] B. J. Levandowski and K. N. Houk, "Theoretical analysis of reactivity patterns in Diels–Alder reactions of cyclopentadiene, cyclohexadiene, and cycloheptadiene with symmetrical and unsymmetrical dienophiles," J. Org. Chem. **80**, 3530 (2015).

[61] J. Sauer, H. Wiest, and A. Mielert, Chem. Ber. **97**, 3183 (1964).

[62] M. Breugst and H. Reissig, "The Huisgen reaction: Milestones of the 1,3-dipolar cycloaddition," Angew. Chem. Int. Ed. **59**, 12293 (2020).

[63] I. Coldham and R. Hufton, "Intramolecular dipolar cycloaddition reactions of azomethine ylides," Chem. Rev. **105**, 2765 (2005).

[64] L. R. Domingo, E. Chamorro, and P. Perez, "Understanding the high reactivity of the azomethine ylides in [3 + 2] cycloaddition reactions," Lett. Org. Chem. **7**, 432 (2010).

[65] L. R. Domingo and S. R. Emamian, "Understanding the mechanisms of [3+2] cycloaddition reactions. The pseudoradical versus the zwitterionic mechanism," Tetrahedron **70**, 1267 (2014).

[66] L. Du, J. You, K. M. Nicholas, and R. H. Cichewicz, "Chemore-active natural products that afford resistance against disparate antibiotics and toxins," Angew. Chem. Int. Ed. **128**, 4292 (2016).

[67] L. Du, C. Munteanu, J. B. King, D. E. Frantz, and R. H. Cichewicz, "An electrophilic natural product provides a safe and robust odor neutralization approach to counteract malodorous organosulfur metabolites encountered in skunk spray," J. Nat. Prod. **82**, 1989 (2019).

[68] K. M. Nicholas, C. Lander, and Y. Shao, "Computational Evaluation of Potential Molecular Catalysts for Nitrous Oxide Decomposition," Under Review.

[69] J. Yang, Z. Pei, J. Deng, Y. Mao, Q. Wu, Z. Yang, B. Wang, C. M. Aikens, W. Liang, and Y. Shao, "Analysis and Visualization of energy densities. I. Insights from real-time time-dependent density functional theory Simulations," Phys. Chem. Chem. Phys. **22**, 26838 (2020).

[70] Z. Pei, J. Yang, J. Deng, Y. Mao, Q. Wu, Z. Yang, B. Wang, C. M. Aikens, W. Liang, and Y. Shao, "Analysis and visualization of energy densities. II. Insights from linear-response time-dependent density functional theory Calculations," Phys. Chem. Chem. Phys. **22**, 26852 (2020).

[71] A. D. Becke, "A multicenter numerical integration scheme for polyatomic molecules," J. Chem. Phys. **88**, 2547 (1988).

Supporting Information for

"Visualization of Electron Density Changes Along Chemical Reaction Pathways"
Chance Lander, Vardhan Satalkar, Junjie Yang, Xiaoliang Pan, Zheng Pei, Aayushi Chatterji, Chungen Liu,
Kenneth M. Nicholas, Robert H. Cichewicz, Zhibo Yang, and Yihan Shao
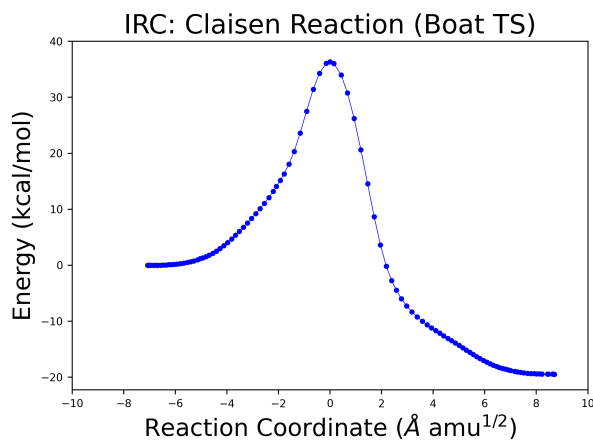
(May 7, 2022)

Figure S1: IRC Pathway for Claisen reaction of allyl vinyl ether *via* boat transition state was obtained using ωB97X-D functional, and 6-31+G* basis set in the gas phase.
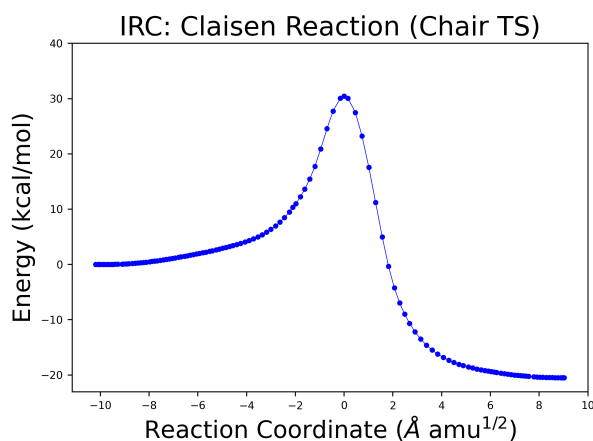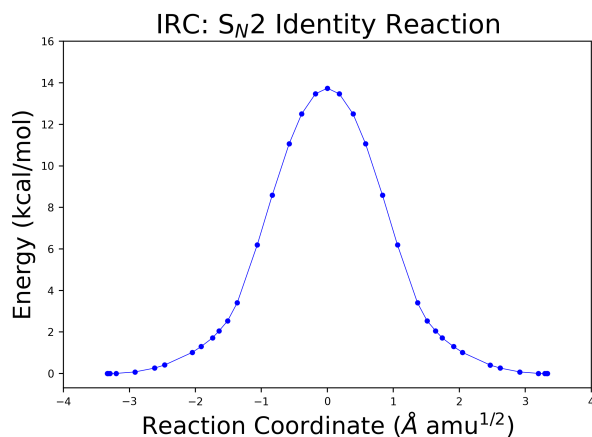

Figure S2: IRC Pathway for Claisen reaction of allyl vinyl ether *via* chair transition state was obtained using ωB97X-D functional, and 6-31+G* basis set in the gas phase.

Figure S3: IRC Pathway for S_N2 identity reaction between methyl chloride and chloride anion was obtained using ωB97X-D functional, and 6-31+G* basis set in the gas phase.
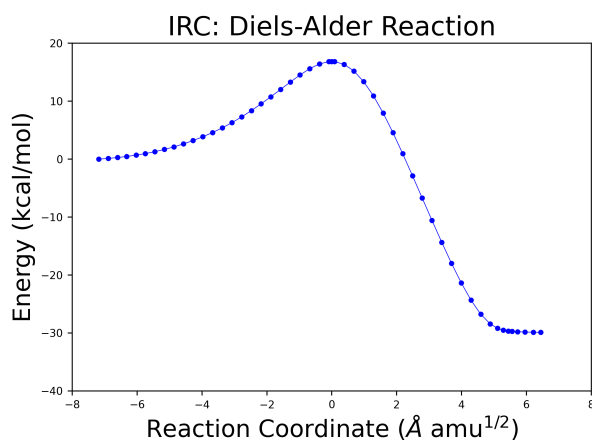

Figure S4: IRC Pathway for Diels-Alder cycloaddition between cyclopentadiene and acrylonitrile was obtained using ωB97X-D functional, and 6-31+G* basis set in the gas phase.
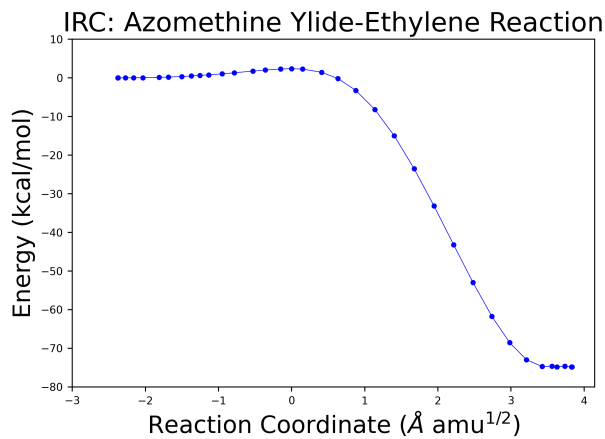

Figure S5: IRC Pathway for azomethine ylide and ethylene cycloaddition was obtained using ωB97X-D functional, and 6-31+G* basis set in the gas phase.
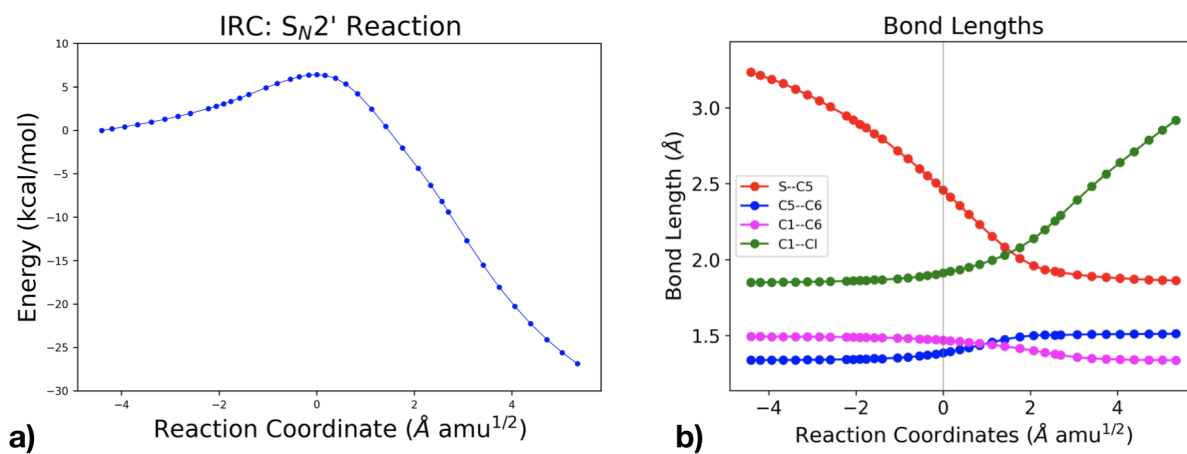
Figure S6: IRC Pathway for S_N2' reaction between pericosine A and phenylethyl mercaptan was obtained using ωB97X-D functional, and 6-31+G* basis set in the gas phase
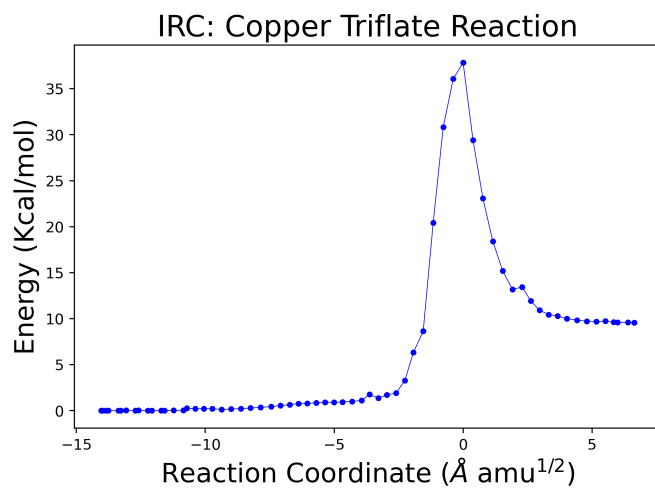

Figure S7: IRC Pathway for spin-crossing splitting of N_2O bound to copper triflate was obtained using ωB97X-D functional, and 6-31+G* basis set in the gas phase